Title
Structural phase diagram and pyroelectric properties of free-standing ferroelectric/non-ferroelectric multilayer heterostructures

Journal
Journal of Applied Physics, 118(24)

ISSN
0021-8979

Authors
Zhang, Jialan
Agar, Josh C
Martin, Lane W

Publication Date
2015-12-28

DOI
10.1063/1.4938116

Peer reviewed

AIP Journal of Applied Physics

Structural phase diagram and pyroelectric properties of free-standing ferroelectric/non-ferroelectric multilayer heterostructures

Jialan Zhang, Josh C. Agar, and Lane W. Martin

Citation: Journal of Applied Physics **118**, 244101 (2015); doi: 10.1063/1.4938116
View online: http://dx.doi.org/10.1063/1.4938116
View Table of Contents: http://scitation.aip.org/content/aip/journal/jap/118/24?ver=pdfcov
Published by the AIP Publishing

Structural phase diagram and pyroelectric properties of free-standing ferroelectric/non-ferroelectric multilayer heterostructures

Jialan Zhang,[1,2] Josh C. Agar,[1,3] and Lane W. Martin[1,3,4]
[1]*Department of Materials Science and Engineering and Materials Research Laboratory, University of Illinois, Urbana-Champaign, Urbana, Illinois 61801, USA*
[2]*Department of Physics and Astronomy, Rutgers University, Piscataway, New Jersey 08854, USA*
[3]*Department of Materials Science and Engineering, University of California-Berkeley, Berkeley, California 94720, USA*
[4]*Materials Science Division, Lawrence Berkeley National Laboratory, Berkeley, California 94720, USA*

(Received 1 October 2015; accepted 6 December 2015; published online 22 December 2015)

Ginzburg-Landau-Devonshire models are used to explore ferroelectric phases and pyroelectric coefficients of symmetric free-standing, thin-film trilayer heterostructures composed of a ferroelectric and two identical non-ferroelectric layers. Using $BaTiO_3$ as a model ferroelectric, we explore the influence of temperature, in-plane misfit strain, and the non-ferroelectric layer (including effects of elastic compliance and volume fraction) on the phase evolution in the ferroelectric. The resulting phase diagram reveals six stable phases, two of which are not observed for thin films on semi-infinite cubic substrates. From there, we focus on heterostructures with non-ferroelectric layers of commonly available scandate materials which are widely used as substrates for epitaxial growth. Again, six phases with volatile phase boundaries are found in the phase diagram for the $NdScO_3/BaTiO_3/NdScO_3$ trilayerheterostructures. The evolution of polarization and pyroelectric coefficients in the free-standing $NdScO_3$ trilayer heterostructures is discussed with particular attention to the role that heterostructure design plays in influencing the phase evolution and temperature-dependence with a goal of creating enhanced pyroelectric response and advantages over traditional thin-film heterostructures. © *2015 AIP Publishing LLC*. [http://dx.doi.org/10.1063/1.4938116]

I. INTRODUCTION

Ferroelectrics[1] exhibit a range of unique properties and have attracted considerable interest for their potential in applications such as thermal sensing/imaging.[2–4] Driven by the desire to fabricate devices on a chip, there has been ongoing interest in the properties of thin-film versions of ferroelectrics and, in turn, a detailed understanding of the fundamental physics of ferroelectric thin films is paramount.[5–7] In this spirit, extensive work on thin-film epitaxy and strain engineering,[8] focusing on ferroelectric films on thick, rigid substrates, has demonstrated that ferroelectric films are strongly influenced by internal strains[9] and can possess phase transformation characteristics in both single-layer[10,11] and multilayer[12] heterostructures that differ significantly from the bulk.

In this study, we focus on a prototypical perovskite ferroelectric $BaTiO_3$ which has Curie temperature $T_C \approx 120\,^{\circ}C$. $BaTiO_3$ undergoes a sequence of phase transitions from cubic to tetragonal to orthorhombic to rhombohedral as the temperature is decreased from its T_C. Previous theoretical studies have investigated the phase transformation characteristics, structures, and ferroelectric nature of the various phases of $BaTiO_3$ single crystals and epitaxial thin films using non-linear thermodynamic models,[13–16] first-principles calculations,[17] and phase-field modeling.[18] Here we focus on phenomenological routes based on Ginzburg-Landau-Devonshire theory to probe this material as an epitaxial, monodomain thin film.

Compared with ferroelectric films on rigid, semi-infinite substrates, thin-film ferroelectrics on a substrate of comparable thickness (i.e., free-standing heterostructures) represent a more nuanced mechanical system whereby the effect of the substrate can be reduced or even removed, and the evolution of strain in the system can be made to depend on the elastic properties of the various layers more equally.[19,20] At the same time, recent success in microfabrication of free-standing complex oxide thin films[21–25] opens the door to potential production, study, and, ultimately, utilization of such free-standing heterostructures. This, in turn, could open new pathways for controlling and optimizing ferroelectric phases, creating phase competition which ultimately can increase susceptibilities (including dielectric, piezoelectric, and pyroelectric responses).

With this in mind, we study the evolution of ferroelectric phases and pyroelectric coefficients of free-standing, non-ferroelectric/$BaTiO_3$/non-ferroelectric trilayer heterostructures, with particular attention to the role of temperature, in-plane misfit strain, and the elastic compliances and volume fractions of the layers in determining the phase evolution and properties. The free-standing trilayer heterostructures were compared to two reference structures: (1) bulk $BaTiO_3$ (volume fraction of ferroelectric = 1) and (2) thin-film $BaTiO_3$ on a rigid, semi-infinite thick substrate (volume fraction of ferroelectric approaching 0). After down-selection of a number of candidate materials, we demonstrate how free-standing $NdScO_3/BaTiO_3/NdScO_3$ heterostructures can provide a pathway to access a diverse range

of near-room-temperature stable phases and provide guidance for the experimental design of multilayers with enhanced pyroelectric coefficients.

II. MODEL AND FORMALISM

We use a thermodynamic formalism based on Ginzburg-Landau-Devonshire theory for a symmetric trilayer system composed of a ferroelectric and two identical non-ferroelectric layers in intimate contact akin to that developed in Ref. 19. The models in this work assume short-circuit boundary conditions in which the polarization mismatch between layers is electrostatically decoupled[26] and the depolarization field can be neglected. It is assumed, for these models, that the presence of the electrodes does not change the mechanical boundary conditions. In this approach, we minimize the free energy with respect to polarization under various stain states and temperatures [Eq. (1)] and using the equilibrium polarization P_i^0 calculate the pyroelectric coefficients π_i [Eq. (2)]

$$\partial G_\Sigma / \partial P_i = 0, \tag{1}$$

$$\pi_i = \frac{dP_i^0}{dT}. \tag{2}$$

In particular, we consider a homogeneous, monodomain, epitaxial ferroelectric $BaTiO_3$ layer in contact with (001)-oriented cubic, non-ferroelectric layers and express the total free energy density of the heterostructure as

$$\begin{aligned} G_\Sigma(P_i, u_m, T) &= \phi_F \cdot G_F + \phi_{NF} \cdot G_{NF} \\ &= \phi_F \cdot [G_0(T) + G_L(T, P_i) \\ &\quad + G_{EL}(P_i, u_m)] + \phi_{NF} \cdot G_{NF}(u_m), \end{aligned} \tag{3}$$

where G_F and G_{NF} are the total energy density of the ferroelectric and non-ferroelectric layers, respectively, G_0 and G_L are the free energy density of the paraelectric and ferroelectric state of the ferroelectric layer, respectively, G_{EL} is the elastic energy density in the ferroelectric layer due to internal strains,[27] u_m is the in-plane misfit strain calculated as $u_m = \frac{a_{NF} - a_F}{a_{NF}}$, a_{NF} and a_F are the equivalent cubic lattice parameters of the non-ferroelectric and ferroelectric layers, respectively, P_i are the components of the polarization vector, T is the temperature, and ϕ_F and ϕ_{NF} are the volume fraction of the ferroelectric and non-ferroelectric layers, respectively (where $\phi_F \approx 0$ and $= 1$ correspond to a ferroelectric thin film on a semi-infinite substrate and a bulk-like ferroelectric, respectively). The general expression of each term of the total free energy density is shown as[28]

$$\begin{aligned} G_L = {} & G_0 + \alpha_1(P_1^2 + P_2^2) + \alpha_3 P_3^2 + \alpha_{11}(P_1^4 + P_2^4) + \alpha_{33} P_3^4 + \alpha_{12} P_1^2 P_2^2 + \alpha_{13}(P_1^2 + P_2^2) P_3^2 \\ & + \alpha_{111}(P_1^6 + P_2^6 + P_3^6) + \alpha_{112}[P_1^2(P_2^4 + P_3^4) + P_2^2(P_1^4 + P_3^4) + P_3^2(P_1^4 + P_2^4)] + \alpha_{123} P_1^2 P_2^2 P_3^2 \\ & + \alpha_{1111}(P_1^8 + P_2^8 + P_3^8) + \alpha_{1112}[P_1^6(P_2^2 + P_3^2) + P_2^6(P_1^2 + P_3^2) + P_3^6(P_1^2 + P_2^2)] \\ & + \alpha_{1122}(P_1^4 P_2^4 + P_2^4 P_3^4 + P_1^4 P_3^4) + \alpha_{1123}(P_1^4 P_2^2 P_3^2 + P_1^2 P_2^4 P_3^2 + P_1^2 P_2^2 P_3^4), \end{aligned} \tag{4}$$

$$G_{EL} = \frac{1}{2} C_{ijkl}(\varepsilon_{ij} - Q_{ijmn} P_m P_n)(\varepsilon_{kl} - Q_{klm'n'} P_{m'} P_{n'}), \tag{5}$$

$$G_{NF} = \frac{1}{2} C_{ijkl} \varepsilon_{ij} \varepsilon_{kl}, \tag{6}$$

where α_i, α_{ij}, α_{ijk}, and α_{ijkl} are dielectric stiffness coefficients, Q_{ijmn} are the cubic electrostriction coefficients, and C_{ijkl} are the cubic elastic stiffness values at constant dielectric displacement. The mechanical boundary conditions are

$$\begin{aligned} & \phi_F \frac{\partial G_F}{\partial \varepsilon_{ij}^F} + \phi_{NF} \frac{\partial G_{NF}}{\partial \varepsilon_{ij}^{NF}} = 0 (i, j = 1, 2), \\ & \frac{\partial G_F}{\partial \varepsilon_{i3}^F} = 0 (i = 1 - 3), \quad \frac{\partial G_F}{\partial \varepsilon_{i3}^{NF}} = 0 (i = 1 - 3), \end{aligned} \tag{7}$$

where $\varepsilon_{ii}^F = \varepsilon_{ii}^{NF} + u_m (i = 1, 2)$, $\varepsilon_{12}^F = \varepsilon_{12}^{NF}$.

The free energy density, achieved by substituting Eqs. (4)–(7) into Eq. (3), is

$$\begin{aligned} G_\Sigma = {} & \phi_F \cdot \{G_0 + \tilde{\alpha}_1(P_1^2 + P_2^2) + \tilde{\alpha}_3 P_3^2 + \tilde{\alpha}_{11}(P_1^4 + P_2^4) + \tilde{\alpha}_{33} P_3^4 + \tilde{\alpha}_{12} P_1^2 P_2^2 + \tilde{\alpha}_{13}(P_1^2 + P_2^2) P_3^2 \\ & + \alpha_{111}(P_1^6 + P_2^6 + P_3^6) + \alpha_{112}[P_1^2(P_2^4 + P_3^4) + P_2^2(P_1^4 + P_3^4) + P_3^2(P_1^4 + P_2^4)] + \alpha_{123} P_1^2 P_2^2 P_3^2 \\ & + \alpha_{1111}(P_1^8 + P_2^8 + P_3^8) + \alpha_{1112}[P_1^6(P_2^2 + P_3^2) + P_2^6(P_1^2 + P_3^2) + P_3^6(P_1^2 + P_2^2)] \\ & + \alpha_{1122}(P_1^4 P_2^4 + P_2^4 P_3^4 + P_1^4 P_3^4) + \alpha_{1123}(P_1^4 P_2^2 P_3^2 + P_1^2 P_2^4 P_3^2 + P_1^2 P_2^2 P_3^4) \\ & + 2\phi_{NF} u_m^2 / [(S_{11}^{NF} + S_{12}^{NF}) \cdot \phi_F + (S_{11}^F + S_{12}^F) \cdot \phi_{NF}]\}, \end{aligned} \tag{8}$$

where $\tilde{\alpha}_i$ and $\tilde{\alpha}_{ij}$ are the renormalized dielectric stiffness coefficients expressed as[19]

$$\tilde{\alpha}_1 = \alpha_1 - \frac{(Q_{11}+Q_{12})\phi_{NF}u_m}{(S_{11}^{NF}+S_{12}^{NF})\cdot\phi_F + (S_{11}^{F}+S_{12}^{F})\cdot\phi_{NF}}, \quad \tilde{\alpha}_3 = \alpha_1 - \frac{2Q_{12}\phi_{NF}u_m}{(S_{11}^{NF}+S_{12}^{NF})\cdot\phi_F + (S_{11}^{F}+S_{12}^{F})\cdot\phi_{NF}}$$

$$\tilde{\alpha}_{11} = \alpha_{11} + \frac{(Q_{11}^2+Q_{12}^2)S_{11}^F - 2Q_{11}Q_{12}S_{12}^F}{2\left[(S_{11}^F)^2-(S_{12}^F)^2\right]} - \frac{(Q_{11}+Q_{12})^2\phi_F(S_{11}^{NF}+S_{12}^{NF})}{4(S_{11}^F+S_{12}^F)\left[(S_{11}^{NF}+S_{12}^{NF})\cdot\phi_F + (S_{11}^F+S_{12}^F)\cdot\phi_{NF}\right]}$$
$$- \frac{(Q_{11}-Q_{12})^2\phi_F(S_{11}^{NF}-S_{12}^{NF})}{4(S_{11}^F-S_{12}^F)\left[(S_{11}^{NF}-S_{12}^{NF})\cdot\phi_F + (S_{11}^F-S_{12}^F)\cdot\phi_{NF}\right]}$$

$$\tilde{\alpha}_{12} = \alpha_{12} + \frac{2Q_{11}Q_{12}S_{11}^F - (Q_{11}^2+Q_{12}^2)S_{12}^F}{(S_{11}^F)^2-(S_{12}^F)^2} + \frac{(Q_{11}-Q_{12})^2\phi_F(S_{11}^{NF}-S_{12}^{NF})}{2(S_{11}^F-S_{12}^F)\left[(S_{11}^{NF}-S_{12}^{NF})\cdot\phi_F + (S_{11}^F-S_{12}^F)\cdot\phi_{NF}\right]}$$
$$- \frac{(Q_{11}+Q_{12})^2\phi_F(S_{11}^{NF}+S_{12}^{NF})}{2(S_{11}^F+S_{12}^F)\left[(S_{11}^{NF}+S_{12}^{NF})\cdot\phi_F + (S_{11}^F+S_{12}^F)\cdot\phi_{NF}\right]} + \frac{Q_{44}^2\phi_{NF}}{2(S_{44}^{NF}\cdot\phi_F + S_{44}^F\cdot\phi_{NF})}$$

$$\tilde{\alpha}_{13} = \alpha_{12} + \frac{(Q_{11}+Q_{12})Q_{12}\phi_{NF}}{\left[(S_{11}^{NF}+S_{12}^{NF})\cdot\phi_F + (S_{11}^F+S_{12}^F)\cdot\phi_{NF}\right]}, \quad \tilde{\alpha}_{33} = \alpha_{11} + \frac{Q_{12}^2\phi_{NF}}{\left[(S_{11}^{NF}+S_{12}^{NF})\cdot\phi_F + (S_{11}^F+S_{12}^F)\cdot\phi_{NF}\right]}. \tag{9}$$

In Voigt notation, Q_{ij} are the electrostrictive coefficients and S_{ij} are the elastic compliances which can be transformed from C_{ij}. In the context of this work, the value S_{ij} is determined by $S_{11}=(C_{11}+C_{12})/(C_{11}-C_{12})(C_{11}+2C_{12})$, $S_{12}=-C_{12}/(C_{11}-C_{12})(C_{11}+2C_{12})$, and $S_{44}=1/C_{44}$. The values of C_{ij} and S_{ij} for various materials are listed in Tables I and II. The Landau coefficients and thermodynamic properties used in Eq. (9) are listed in Table III.[28]

The differences in the dielectric stiffness coefficients [Eq. (9)] in the trilayer heterostructure compared with its bulk ferroelectric counterpart are due to the elastic energy contribution from the non-ferroelectric layers, which depends on ϕ_F and S_{ij}^{NF} (i.e., $S_{11}^{NF}+S_{12}^{NF}$, $S_{11}^{NF}-S_{12}^{NF}$, and S_{44}^{NF} in this study). Our preliminary calculations show that the variation of S_{44} has much less impact on the equilibrium polarization and phases than do $S_{11}^{NF}+S_{12}^{NF}$ and $S_{11}^{NF}-S_{12}^{NF}$ and therefore we will begin our discussion focusing on their influence on the phase evolution and pyroelectric response.

III. RESULTS AND DISCUSSION

A schematic of the non-ferroelectric/ferroelectric/non-ferroelectric trilayer heterostructure and the associated parameters is provided [Figure 1(a)]. The model used incorporates a number of parameters including the Landau coefficients and thermodynamic properties of the ferroelectric layer, elastic compliance of the non-ferroelectric layers ($S_{11}^{NF}+S_{12}^{NF}$ and $S_{11}^{NF}-S_{12}^{NF}$), the volume fractions of the ferroelectric [ϕ_F] and non-ferroelectric [$\phi_{NF}=1-\phi_F$] layers, as well as the temperature and misfit strain. Here we fix the parameters for the ferroelectric layer to be those of $BaTiO_3$ (Table III).

We obtain the temperature–misfit strain phase diagram for epitaxial, monodomain $BaTiO_3$ films on semi-infinite, non-ferroelectric substrates [Figure 1(b)] with the range of misfit strain from $-0.003 \le u_m \le 0.003$ and temperatures from $0\,^\circ\text{C} \le T \le 150\,^\circ\text{C}$. Four stable phases are observed: (1) paraelectric (p; $P_1=P_2=P_3=0$), (2) tetragonal with polarization along [001] (c; $P_1=P_2=0$, $P_3\neq 0$), (3) orthorhombic with polarization along [110] (aa; $|P_1|=|P_2|\neq 0$, $P_3=0$), and (4) rhombohedral with the polarization along [111] (r; $|P_1|=|P_2|\neq 0$, $P_3\neq 0$), all of which are consistent with those reported previously.[15] Although not overly important, it should be noted that the symmetry of the r phase in epitaxial films could be slightly distorted from its bulk equivalent. For the same range of temperatures and misfit strain, we also calculated the temperature–misfit strain phase

TABLE I. Elastic stiffness (unit: 10^{11} N/m^2) of various oxides.

	C_{11}	C_{12}	C_{44}
$BaTiO_3$[28]	1.78	0.964	1.22
$CoFe_2O_4$[33]	2.57	1.50	0.85
MgO[34]	2.959	0.954	1.539
$CoAl_2O_4$[33]	2.905	1.703	1.38
$SrTiO_3$[28]	3.181	1.025	1.215
$LaAlO_3$[35]	3.37	1.51	1.21
$NdScO_3$[36]	3.079	1.467	1.078
$GdScO_3$[37]	2.94	1.63	1.03
$DyScO_3$[38]	3.024	1.244	1.039

TABLE II. Elastic compliances (unit: 10^{-12} m^2/N) of various oxides with relations between S_{ij} and C_{ij} in this work, $S_{11}=\frac{(C_{11}+C_{12})}{(C_{11}-C_{12})(C_{11}+2C_{12})}$, $S_{12}=\frac{-C_{12}}{(C_{11}-C_{12})(C_{11}+2C_{12})}$, and $S_{44}=\frac{1}{C_{44}}$.

	S_{11}	S_{12}	$S_{11}+S_{12}$	S_{11}-S_{12}	S_{44}
$BaTiO_3$[28]	9.069	−3.186	5.882	12.255	8.197
$CoFe_2O_4$[33]	6.829	−2.517	4.312	9.346	11.765
MgO[34]	4.010	−0.978	3.032	4.988	6.498
$CoAl_2O_4$[33]	6.074	−2.245	3.829	8.319	7.246
$SrTiO_3$[28]	3.729	−0.909	2.820	4.638	8.230
$LaAlO_3$[35]	4.106	−1.270	2.836	5.376	8.264
$NdScO_3$[36]	4.690	−1.513	3.177	6.203	9.276
$GdScO_3$[37]	5.627	−2.007	3.620	7.634	9.709
$DyScO_3$[38]	4.350	−1.268	3.082	5.618	9.625

TABLE III. Thermodynamic and elastic coefficients of $BaTiO_3$ (temperature T in °C).[28]

α_1 (10^5 m^2 N/C^2)	4.124 ($T-115$)	α_{1122} (10^{10} m^{14} N/C^8)	1.637
α_{11} (10^8 m^6 N/C^4)	−2.097	α_{1123} (10^{10} m^{14} N/C^8)	1.367
α_{12} (10^8 m^6 N/C^4)	7.794	Q_{11} (m^4/C^2)	0.1
α_{111} (10^9 m^{10} N/C^6)	1.294	Q_{12} (m^4/C^2)	−0.034
α_{112} (10^9 m^{10} N/C^6)	−1.950	C_{11} (10^{11} N/m^2)	1.78
α_{123} (10^9 m^{10} N/C^6)	−2.5	C_{12} (10^{11} N/m^2)	0.964
α_{1111} (10^{10} m^{14} N/C^8)	3.863	C_{44} (10^{11} N/m^2)	1.22
α_{1112}(10^{10} m^{14} N/C^8)	2.529		

diagram for free-standing epitaxial, monodomain non-ferroelectric/$BaTiO_3$/non-ferroelectric trilayer heterostructures assuming equal elastic compliances and volume fractions of the layers (i.e., $S_{ij}^{F} = S_{ij}^{NF}$, and $\phi_F = 0.5$) [Figure 1(c)]. Consistent with previous studies,[19] two new phases are found: (1) tetragonal with polarization along [100] or [010] (a; $P_1 \neq 0$, $P_2 = P_3 = 0$ or $P_1 = P_3 = 0$, $P_2 \neq 0$, respectively) and (2) orthorhombic with polarization along [101] or [011] (ac; $|P_1| \neq 0$, $|P_2| = 0$, and $P_3 \neq 0$ or $|P_1| = 0$, $|P_2| \neq 0$, and $P_3 \neq 0$). This demonstrates that the free-standing multilayer heterostructures provide the possibility for phases with anisotropic, in-plane polarization to be produced, which are known to be difficult to stabilize for thin films on thick, cubic substrates. Additionally, the stability range for the c phase in the free-standing trilayer heterostructure extends from compressive strains into small tensile strains and potentially can be further tuned by selection of the non-ferroelectric layers.

The volume fraction–misfit strain phase diagram, at $T = 25$ °C within the misfit strain range from $-0.003 \leq u_m \leq 0.003$ and volume fractions from $0 \leq \phi_F \leq 1$, has also been calculated for the epitaxial, monodomain non-ferroelectric/$BaTiO_3$/non-ferroelectric trilayer heterostructures assuming equal elastic compliances between the layers (i.e., $S_{ij}^{F} = S_{ij}^{NF}$) [Figure 2(a)]. In this case, five stable phases are found. Under relatively large compressive strains, the stable phase is always the c phase, independent of ϕ_F and u_m; that stability range also extends to small tensile strains as ϕ_F increases. As one moves into the small compressive and tensile strain regime, the phase diagram becomes more complicated and competition between five ferroelectric phases a, aa, ac, c, and r is observed. In this regime, in general, as ϕ_F increases, the effect of the non-ferroelectric layers on the ferroelectric layer decreases, resulting in the stabilization of a and ac phases. At $\phi_F \approx 1$, the stable phases in the diagram correspond to those of bulk-like $BaTiO_3$. Thus, by varying both the volume fraction and the misfit strain within the free-standing non-ferroelectric/ferroelectric/non-ferroelectric trilayer heterostructures, one can provide an interesting pathway to manipulate the phase of the $BaTiO_3$.

In the phase diagrams we have studied thus far, we have assumed equal elastic compliances of the layers (i.e., $S_{ij}^{F} = S_{ij}^{NF}$). From here, we can also proceed to explore the evolution of phase diagrams under an assumption of equal volume fractions (i.e., $\phi_F = 0.5$) with changing elastic compliances of the non-ferroelectric layers ($S_{11}^{NF} + S_{12}^{NF}$) and misfit strain ($u_m$). The larger the magnitude of S_{ij}, the more compliant (i.e., less stiff) the material is.[29] In this study, it is convenient to analyze the effect of compliances of the non-ferroelectric materials using the two parameters $S_{11}^{NF} + S_{12}^{NF}$ and $S_{11}^{NF} - S_{12}^{NF}$ [Eq. (7)]. In this spirit, we provide phase diagrams at two values of $S_{11}^{NF} - S_{12}^{NF}$ (12.25×10^{-12} m^2/N [Figure 2(b)] and 5.38×10^{-12} m^2/N [Figure 2(c)]) across a range of $S_{11}^{NF} + S_{12}^{NF}$ from 0–8 $\times 10^{-12}$ m^2/N, based on the magnitudes of S_{ij} we obtained from a survey of oxide materials [Tables I and II]. It is found in both cases [Figures 2(b) and 2(c)], unsurprisingly, that c and aa are the equilibrium phases at large compressive or tensile strain, respectively, regardless of the compliances of the non-ferroelectric layers. As in the previous case studied above, the ac and r phases are only stable at small or intermediate

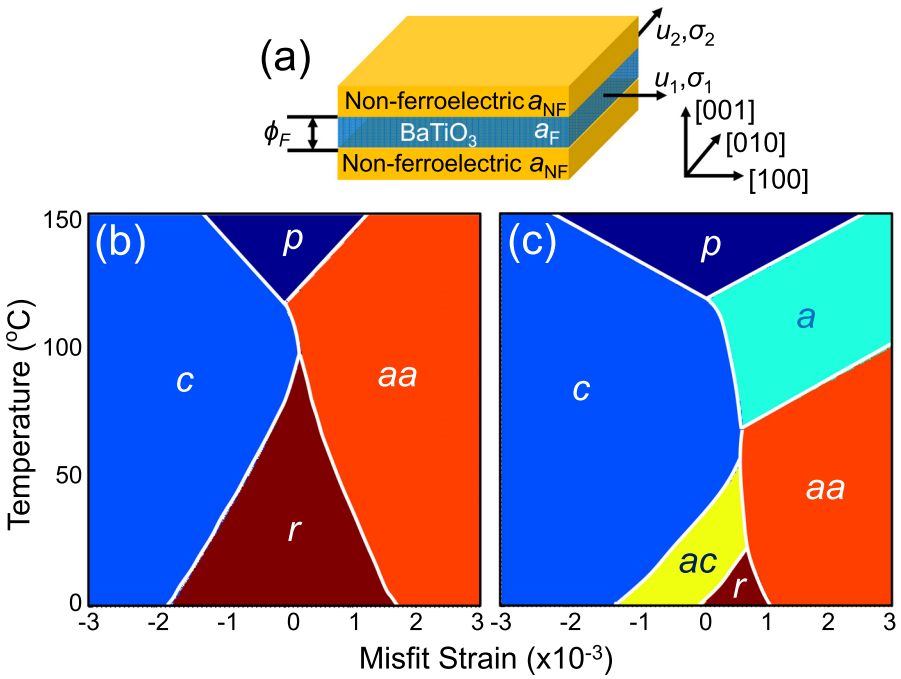

FIG. 1. (a) Schematic of the non-ferroelectric/ferroelectric/non-ferroelectric trilayer heterostructure. Temperature–misfit strain phase diagram of $BaTiO_3$ films on (b) semi-infinite substrates ($\phi_F \approx 0$) and (c) substrates with the same thickness with the film ($\phi_F = 0.5$) assuming equal elastic compliances between layers ($S_{ij}^{F} = S_{ij}^{NF}$).

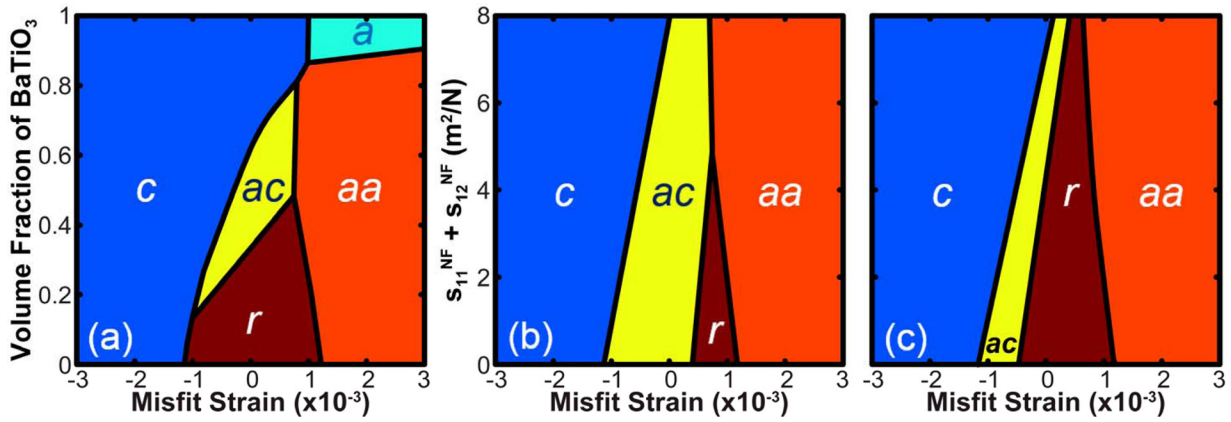

FIG. 2. (a) Volume fraction–misfit strain phase diagram of non-ferroelectric/$BaTiO_3$/non-ferroelectric free-standing trilayer heterostructure at $T = 25\,^{\circ}C$ assuming equivalent elastic compliances between the layers ($S_{ij}^{F} = S_{ij}^{NF}$). Elastic compliance–misfit strain phase diagram of non-ferroelectric/$BaTiO_3$/non-ferroelectric free-standing trilayer heterostructure for (b) $S_{11}^{NF} - S_{12}^{NF} = 12.25 \times 10^{-12}\ m^2/N$ and (c) $S_{11}^{NF} - S_{12}^{NF} = 5.38 \times 10^{-12}\ m^2/N$ with equal layer thickness ($\phi_F = 0.5$) at $T = 25\,^{\circ}C$.

strains. For the same magnitude of $S_{11}^{NF} - S_{12}^{NF}$, the ranges of strains where *ac* and *r* phases are stable shrink as the non-ferroelectric layers are made more compliant (i.e., larger magnitude of $S_{11}^{NF} + S_{12}^{NF}$). Comparing the two diagrams associated with the two values of $S_{11}^{NF} - S_{12}^{NF}$, it is observed that the phase boundary between the *ac* and *r* phases shifts as a function of $S_{11}^{NF} - S_{12}^{NF}$, while the phase boundaries between the *c*/*ac* and *r*/*aa* phases are essentially independent of $S_{11}^{NF} - S_{12}^{NF}$. This can be explained by the fact that the magnitude of $S_{11}^{NF} - S_{12}^{NF}$ represents the difference in compliances between two orthogonal in-plane axes of the non-ferroelectric layers [Figure 1(a)] and provides information on how misfit strain can be different along the two in-plane directions. The bigger that difference, the more likely the ferroelectric phase is to possess unequal polarization components along the two in-plane directions. Therefore, as the magnitude of $S_{11}^{NF} - S_{12}^{NF}$ increases, for the same magnitude of $S_{11}^{NF} + S_{12}^{NF}$, the stability regime of the *r* phase, with isotropic in-plane polarization, is reduced and the stability of the *ac* phase, with anisotropic in-plane polarization, is enhanced.

From these results, it is clear that the majority of the complexity and potential for interesting, near-phase-boundary effects, which generally have enhanced susceptibilities, will be found in the small strain regime in $BaTiO_3$-based free-standing trilayer heterostructures. From here, we have examined the lattice parameters of a variety of commercially available substrates (these materials were considered because they are commonly used in the community and the elastic constants are typically measured for these systems, thereby enabling reliable usage in these models) and find that those of $NdScO_3$ ($a = 5.770$ Å, $b = 5.579$ Å, and $c = 7.999$ Å; corresponding to a pseudocubic lattice parameter of 4.008 Å)[8,30] allow for maintenance of very small lattice misfit strain (0.075%) with $BaTiO_3$ (with lattice parameter of 4.005 Å) and thus ready access to the regime of near-room-temperature enhanced properties. We note that the appropriate elastic constants are not necessarily available for a large number of candidate perovskite materials, thus limiting our survey in some regard. Additionally, we focus on perovskite systems because practical construction of these heterostructures would require the ability to create high-quality heterostructures which requires materials with chemical and structural compatibility to the ferroelectric layer. In this regard, $NdScO_3$ is a good material because it possesses a perovskite structure and is known to enable the growth of high-quality, multilayer structures.

Based on this observation, we have gone on to down-select to study the phase diagram for (001)-oriented $NdScO_3$/$BaTiO_3$/$NdScO_3$ free-standing trilayer heterostructures as a function of temperature and volume fraction of the $BaTiO_3$. Calculation of the volume fraction–temperature phase diagram [Figure 3(a)] reveals that all six phases noted above are found to be stable in the $NdScO_3$/$BaTiO_3$/$NdScO_3$ free-standing trilayer heterostructures. For relatively small ϕ_F, the *r* phase is stable in the temperature range from 0 to 50 °C, and the phase evolves with increasing temperature from $r \rightarrow aa \rightarrow p$ and from $r \rightarrow aa \rightarrow a \rightarrow p$ with the former occurring at a small ϕ_F and the latter at larger ϕ_F. As ϕ_F increases further, the effect of the $NdScO_3$ layers on the $BaTiO_3$ layer decreases, resulting in a multiplicity of equilibrium phases including *r*, *aa*, *ac*, *a*, and *c* phases as temperature is varied. For all magnitudes of ϕ_F at $T \geq 136\,^{\circ}C$, the polarization is found to be entirely suppressed, corresponding to the *p* phase in the diagram. The choice of non-ferroelectric layers is critical for obtaining such phase competition. For comparison, if one calculates the phase diagram using other non-ferroelectric layers, for instance we calculated for both $DyScO_3$ and $GdScO_3$ non-ferroelectric layers, the volume fraction–temperature phase diagram of those free-standing heterostructures reveals that only the *c* phase is stable with the range of misfit strain from $-0.003 \leq u_m \leq 0.003$ and temperatures from $0\,^{\circ}C \leq T \leq 150\,^{\circ}C$. In general, it should be possible to choose from a range of possible non-ferroelectric layers and, if one controls things like the lattice parameter, the elastic constants, the thermal expansion mismatch, etc., one can potentially exert considerable control on the system. The current study is in no way meant to be an exhaustive study, but only demonstrates the concept with known materials.

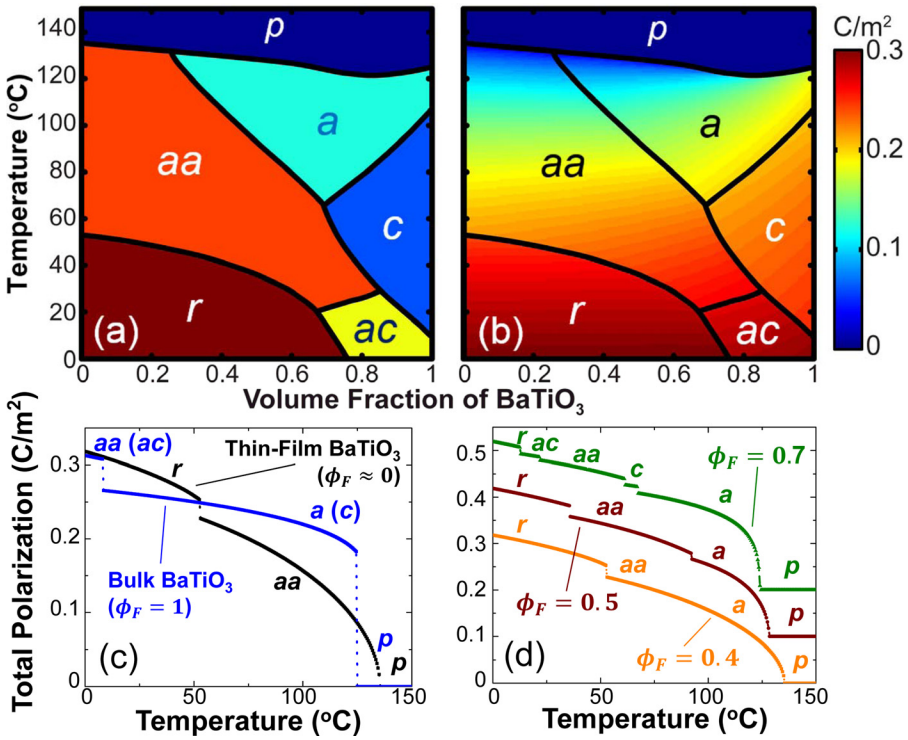

FIG. 3. Temperature–volume fraction (a) ferroelectric phase diagram and (b) total equilibrium polarization of a $NdScO_3/BaTiO_3/NdScO_3$ trilayer heterostructure. Equilibrium polarization as a function of temperature for $NdScO_3/BaTiO_3/NdScO_3$ trilayer heterostructures of (c) $\phi_F \approx 0$ and 1 and (d) $\phi_F = 0.4$, 0.5, and 0.7 with the origin of the vertical axis coordinate at 0, 0.1, and 0.2 C/m^2, respectively.

In order to better understand the characteristics of these various phase transitions, the magnitude of the total equilibrium polarization as a function of temperature and volume fraction of $BaTiO_3$ was calculated [Figure 3(b)] and, to illustrate the nature of the phase transitions, temperature-dependent slices at $\phi_F \approx 0$, 1 [Figure 3(c)] and $\phi_F = 0.4$, 0.5, and 0.7 [Figure 3(d)] are provided. For $\phi_F \approx 0$ (i.e., thin-film $BaTiO_3$ on a semi-infinite $NdScO_3$ substrate), the phase sequence with increasing temperature is the same as those shown before [Figure 1(a)], $r \rightarrow aa \rightarrow p$ in which the $r \rightarrow aa$ and $aa \rightarrow p$ phase transitions are weakly 1st and 2nd order, respectively. For $\phi_F = 1$ (i.e., akin to bulk-like $BaTiO_3$), the phase sequence with increasing temperature is *ac* (*aa*) → *c* (*a*) → *p* in which *ac* (*aa*) → *c* (*a*) and *c* (*a*) → *p* phase transitions are weakly and strongly 1st order, respectively. From here, we can explore what happens at three intermediate volume fraction values ($\phi_F = 0.4$, 0.5, and 0.7) to illustrate some of the phase transitions present in this system. $\phi_F = 0.7$, in particular, is the volume fraction at which the most phase transitions occur in the diagram [Figure 3(d)]. The three curves in Figure 3(d) are shown in such a way that the coordinate where total polarization is zero for the orange ($\phi_F = 0.4$), red ($\phi_F = 0.5$), and green ($\phi_F = 0.7$) curves corresponds to 0, 0.1, and 0.2 C/m^2 on the vertical axis, respectively. At $\phi_F = 0.5$, the phase sequence with increasing temperature is $r \rightarrow aa \rightarrow a \rightarrow p$ [red curve, Figure 3(d)]. Note that this phase sequence is different from that reported in Figure 1(c), because of the fact that $NdScO_3$ ($S_{11} = 4.69$ m^2/N, $S_{12} = -1.513$ m^2/N) is less compliant than $BaTiO_3$ (Table II), while the compliance of the layers in Figure 1(c) was assumed to be equivalent. Likewise, if one reduces the fraction of $BaTiO_3$ ($\phi_F = 0.4$), allowing the $NdScO_3$ to have a greater impact on the structure, the stability ranges of the *r* and *aa* phases are extended [orange curve, Figure 3(d)]. On the other hand, increasing the volume fraction of the $BaTiO_3$ ($\phi_F = 0.7$) reduces the influence of the $NdScO_3$, resulting in a more complex phase evolution containing additional *ac* and *c* phases [green curve, Figure 3(d)].

Such a complex phase diagram could, in turn, be advantageous for the design of high-performance pyroelectric responses in the system since near phase boundaries these susceptibilities are generally enhanced. We have separately calculated the pyroelectric coefficients under zero electrical field along all three cardinal directions of the lattice ([100], [010], and [001], respectively) [Figures 4(a)–4(c)]. For the pyroelectric coefficient (π_i) along [100] [Figure 4(a)], the largest pyroelectric coefficient occurs in the temperature range from 115 to 135 °C and across all ϕ_F. The magnitude of the largest pyroelectric coefficient is found to be at ϕ_F close to 1. For the pyroelectric coefficient along [010] [Figure 4(b)], in contrast, has the largest pyroelectric coefficients in the regime from 100 to 135 °C within a much narrower range of ϕ_F from 0–0.5. This result is primarily due to the absence of polarization and therefore pyroelectric coefficient along [010] in the *a* phase. The magnitude of the pyroelectric coefficients along both [100] and [010] remains ≥ 0.002 C/m^2 °C even as the temperature is decreased by 40–50 °C from the Curie temperatures a relatively wide temperature range to observe such a large pyroelectric response. For the pyroelectric coefficient along [001] [Figure 4(c)], the largest pyroelectric coefficient is found in the regime from 40 to 50 °C, within the range of ϕ_F from 0 to 0.4. The temperature range where the pyroelectric coefficient along [001] is ≥ 0.002 C/m^2 °C K is narrower and only extends to about 5 °C below the Curie temperature. At constant ϕ_F, the magnitude of the pyroelectric coefficients along each of the three directions reaches a maximum within a very narrow temperature resulting in a phase boundary where the value of dP_i/dT

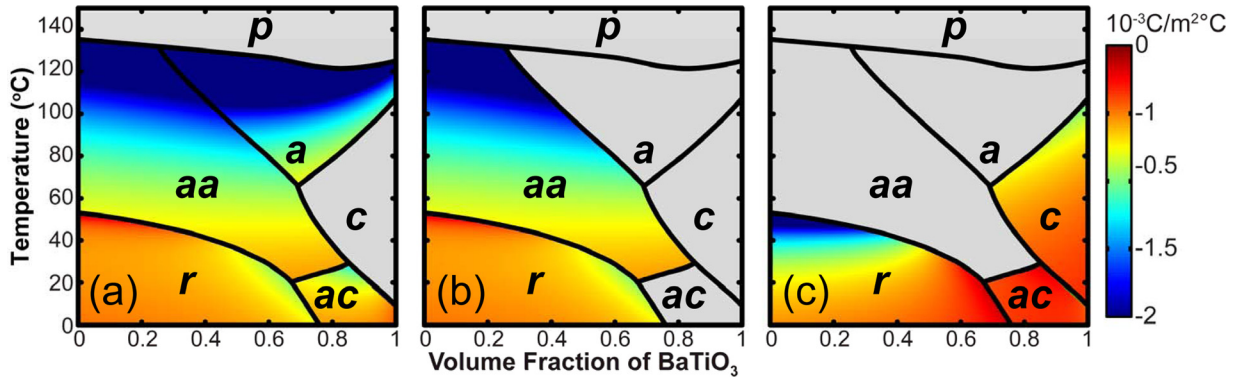

FIG. 4. Pyroelectric coefficients as functions of temperature and volume fraction along (a) [100], (b) [010], and (c) [001] of the $NdScO_3/BaTiO_3/NdScO_3$ trilayer heterostructures.

is quite large.[31] At $T = 25\,^{\circ}C$, the magnitude of the pyroelectric coefficients along the three directions, in general, is found to be in the range from 0.2×10^{-3} to 1.0×10^{-3} $C/m^2\,^{\circ}C$ K. In contrast to bulk $BaTiO_3$,[32] the pyroelectric responses of free-standing $NdScO_3/BaTiO_3/NdScO_3$ trilayer heterostructures [Figure 4] exhibit a relatively wide temperature range for large pyroelectric response and the flexibility to adjust the volume fraction of the layers enables one to be able to tune the temperature of the maximum pyroelectric response from $>100\,^{\circ}C$ down to as low as room temperature.

IV. CONCLUSIONS

We have investigated free-standing non-ferroelectric/ferroelectric/non-ferroelectric trilayer heterostructures using a nonlinear thermodynamic model. Using $BaTiO_3$ as the ferroelectric layer, we explored the phase diagram as a function of temperature, in-plane misfit strain, and the elastic compliances and volume fraction of the non-ferroelectric layers. In the phase diagram of the $BaTiO_3$-based, free-standing trilayer heterostructures, six phases are found to be stable, two of which are not observed for thin films on semi-infinite cubic substrates. The new *a* and *ac* phases appear at relatively large volume fractions of the non-ferroelectric layers and at small or intermediate strains. The range of strains where *ac* and *r* phases are stable is made smaller as the non-ferroelectric layers are made more compliant, while only the phase boundary between *ac* and *r* phases shifts as a function of the differences in compliances between two orthogonal in-plane axes of each layer. All six phases with volatile phase boundaries are found in the phase diagram for $NdScO_3/BaTiO_3/NdScO_3$ trilayer heterostructure. The evolution of polarization and phase sequences as a function of temperature and volume fraction of the layers are demonstrated and compared with bulk $BaTiO_3$ and $BaTiO_3$ films on semi-infinite $NdScO_3$ substrates. Relatively large pyroelectric susceptibilities are found in $NdScO_3/BaTiO_3/NdScO_3$ trilayer heterostructure within specific temperature and volume fraction ranges. These results provide a pathway to access stable ferroelectric phases and to guide experimental design of multilayers with potentially new phases which can produce pyroelectric responses not possible in heterostructures with semi-infinite non-ferroelectric layers.

ACKNOWLEDGMENTS

J.Z. acknowledges support from the National Science Foundation under grant CMMI-1434147, J. C. A. acknowledges support from the National Science Foundation under grant DMR-1451219, and L. W. M. acknowledges support from the Army Research Office under grant W911NF-14-1-0104.

[1]R. E. Cohen, Nature **358**, 136 (1992).
[2]R. W. Whatmore, Rep. Prog. Phys. **49**, 1335 (1986).
[3]R. Watton, Ferroelectrics **91**, 87 (1989).
[4]S. P. Alpay, J. Mantese, S. Trolier-McKinstry, Q. Zhang, and R. W. Whatmore, MRS Bull. **39**, 1099 (2014).
[5]N. Setter, D. Damjanovic, L. Eng, G. Fox, S. Gevorgian, S. Hong, A. Kingon, H. Kohlstedt, N. Y. Park, G. B. Stephenson, I. Stolitchnov, A. K. Tagantsev, D. V. Taylor, T. Yamada, and S. Streiffer, J. Appl. Phys. **100**, 051606 (2006).
[6]M. Dawber, K. M. Rabe, and J. F. Scott, Rev. Mod. Phys. **77**, 1083 (2005).
[7]P. Muralt, J. Micromech. Microeng. **10**, 136 (2000).
[8]D. G. Scholom, L.-Q. Chen, C.-B. Eom, K. M. Rabe, S. K. Streiffer, and J.-M. Triscone, Annu. Rev. Mater. Res. **37**, 589 (2007).
[9]J. Karthik, A. R. Damodaran, and L. W. Martin, Adv. Mater. **24**, 1610 (2012).
[10]Q. Y. Qiu, R. Mahjoub, S. P. Alpay, and V. Nagarajan, Acta Mater. **58**, 823 (2010).
[11]Q. Y. Qiu, V. Nagarajan, and S. P. Alpay, Phys. Rev. B **78**, 064117 (2008).
[12]R. Mahjoub, S. P. Alpay, and V. Nagarajan, Phys. Rev. Lett. **105**, 197601 (2010).
[13]N. A. Pertsev, A. G. Zembilgotov, and A. K. Tagantsev, Phys. Rev. Lett. **80**, 1988 (1998).
[14]I. B. Misirlioglu, S. P. Alpay, F. He, and B. O. Wells, J. Appl. Phys. **99**, 104103 (2006).
[15]V. B. Shirokov, Y. I. Yuzyuk, B. Dkhil, and V. V. Lemanov, Phys. Rev. B **75**, 224116 (2007).
[16]J. Zhang, A. A. Heitmann, S. P. Alpay, and G. A. Rossetti, Jr., J. Mater. Sci. **44**, 5263 (2009).
[17]O. Dieguez, S. Tinte, A. Antons, C. Bungaro, J. B. Neaton, K. M. Rabe, and D. Vanderbilt, Phys. Rev. B **69**, 212101 (2004).
[18]Y. L. Li, L. E. Cross, and L. Q. Chen, J. Appl. Phys. **98**, 064101 (2005).
[19]S. Prokhorenko and N. A. Pertsev, J. Appl. Phys. **110**, 074116 (2011).
[20]S. Prokhorenko, H. Kohlstedt, and N. A. Pertsev, J. Appl. Phys. **116**, 114107 (2014).
[21]L. Pellegrino, M. Biasotti, E. Bellingeri, C. Bernini, A. S. Siri, and D. Marré, Adv. Mater. **21**, 2377 (2009).
[22]Q. Gan, R. A. Rao, C. B. Eom, J. L. Garrett, and M. Lee, Appl. Phys. Lett. **72**, 978 (1998).
[23]J.-H. Kim and A. M. Grishin, Appl. Phys. Lett. **87**, 033502 (2005).
[24]H. W. Jang, S. H. Baek, D. Ortiz, C. M. Folkman, C. B. Eom, Y. H. Chu, P. Shafer, R. Ramesh, V. Vaithyanathan, and D. G. Schlom, Appl. Phys. Lett. **92**, 062910 (2008).

[25]S. H. Baek, J. Park, D. M. Kim, V. A. Aksyuk, R. R. Das, S. D. Bu, D. A. Felker, J. Lettieri, V. Vaithyanathan, S. S. N. Bharadwaja, N. Bassiri-Gharb, Y. B. Chen, H. P. Sun, C. M. Folkman, H. W. Jang, D. J. Kreft, S. K. Streiffer, R. Ramesh, X. Q. Pan, S. Trolier-McKinstry, D. G. Schlom, M. S. Rzchowski, R. H. Blick, and C. B. Eom, Science **334**, 958 (2011).
[26]F.-C. Sun, M. T. Kesim, Y. Espinal, and S. P. Alpay, J. Mater. Sci. **51**, 499 (2016).
[27]G. Akcay, S. P. Alpay, G. A. Rossetti, Jr., and J. F. Scott, J. Appl. Phys. **103**, 024104 (2008).
[28]L. Q. Chen, in *Physics of Ferroelectrics a Modern Perspective*, Topics in Applied Physics Vol **105**, edited by K. Rabe, Ch. H. Ahn, and J.-M. Triscone (Springer-Verlag, Berlin, 2007).
[29]J. F. Nye, *Physical Properties of Crystals* (Oxford University Press, 1985).
[30]J. Schubert, O. Trithaveesak, A. Petraru, C. L. Jia, R. Uecker, P. Reiche, and D. G. Schlom, Appl. Phys. Lett. **82**, 3460 (2003).
[31]J. Zhang, M. W. Cole, and S. P. Alpay, J. Appl. Phys. **108**, 054103 (2010).
[32]T. A. Perls, T. J. Diesel, and W. I. Dobrov, J. Appl. Phys. **29**, 1297 (1958).
[33]Z. Li, E. S. Fisher, J. Z. Liu, and M. V. Nevitt, J. Mater. Sci. **26**, 2621 (1991).
[34]K. Marklund and S. A. Mahmoud, Phys. Scr. **3**, 75 (1971).
[35]X. Luo and B. Wang, J. Appl. Phys. **104**, 073518 (2008).
[36]K. A. Pestka II, E. S. Scott, and Y. L. Page, AIP Advances **1**, 032154 (2011).
[37]K. A. Pestka II, J. D. Maynard, A. Soukiassian, X. X. Xi, D. G. Scholom, Y. L. Page, M. Bernhagen, P. Reiche, and R. Uecker, Appl. Phys. Lett. **92**, 111915 (2008).
[38]M. Janovska, P. Sedlak, H. Seiner, M. Landa, P. Marton, P. Ondrejkovic, and J. Hlinka, J. Phys.: Condens. Matter **24**, 385404 (2012).